processes

MDPI

Article

Bubble Migration Velocity Model for Ultra-Deep Highly Deviated and Horizontal Wells

Xuliang Zhang [1,2], Yunhu Lu [1,*], Hao Qin [2] and Hongxing Yuan [3]

[1] School of Petroleum Engineering, China University of Petroleum (Beijing), Beijing 102249, China
[2] PetroChina Tarim Oilfield Company, Korla City 841000, China
[3] School of Petroleum Engineering, China University of Petroleum (East China), Dongying 266580, China
* Correspondence: luyh@cup.edu.cn

Abstract

Deep and ultra-deep reservoirs are increasingly important, while gas kicks remain a major well-control risk. Accurate prediction of gas migration velocity across different wellbore inclinations is essential for locating the influx front, enabling timely kick detection, and optimizing well-killing procedures. Owing to pressure and temperature variations along the wellbore, the same influx gas may change from a highly compressed, relatively high-density state near the bottomhole to a lower-density, conventional gas-like state as it migrates upward. Accordingly, air bubbles and kerosene droplets were used to represent conventional and highly compressed gas, respectively. Adjustable-inclination annular experiments investigated CMC-controlled viscosity in bubble tests and HCOOK-induced coupled changes in density and viscosity in droplet tests. With increasing inclination, both dispersed phases became increasingly deformed. Bubble migration velocity decreased monotonically with viscosity and inclination, whereas droplet velocity first increased and then decreased, peaking at 15–30°. Along the tested HCOOK formulation path, droplet velocity varied non-monotonically. Based on 155 bubble observations and 75 droplet observations, separate correlations were integrated into a combined gas-migration model. Validation against three field wells yielded absolute relative errors of 8.75–11.20%, demonstrating its practical value for estimating field gas migration velocities.

Keywords: ultra-deep wells; highly deviated and horizontal wells; gas migration velocity model; gas kick; multiphase flow

1. Introduction

China has abundant deep and ultra-deep oil and gas resources with substantial development potential. The development of these resources is of great significance for optimizing the national energy structure and ensuring energy security [1]. As exploration and development extend to greater depths, drilling and completion increasingly encounter difficult formations, instability in long open-hole sections, frequent influx and lost-circulation events, and more severe high-temperature, high-pressure, and corrosive downhole conditions. These challenges constrain the cost-effective development of oil and gas fields [2]. During ultra-deep drilling, gas influxes can readily occur because of high temperature, high pressure, high stress, and complex formation conditions [3]. Compared with vertical wells, ultra-deep highly deviated and horizontal wells have horizontal sections and long inclined sections, making gas influx more difficult to detect. If not detected and handled in a timely

Check for updates

Academic Editor: Tianshou Ma

Received: 7 September 2026
Revised: 26 September 2026
Accepted: 29 September 2026
Published: 30 September 2026

Copyright: © 2026 by the authors. Licensee MDPI, Basel, Switzerland. This article is an open access article distributed under the terms and conditions of the Creative Commons Attribution (CC BY) license.

manner, the influx may worsen, increasing well control risks. Therefore, understanding how influx gas migrates after entering the wellbore is particularly important.

Bubble migration studies can be broadly grouped according to the effects of wellbore inclination, fluid properties, and the applicable flow regime. Regarding inclination, experimental and numerical studies consistently show that changes in pipe orientation affect both bubble migration velocity and morphology, although the reported velocity trends are not universal. Shosho et al. [4], Massoud et al. [5], and Boucher et al. [6] observed a non-monotonic dependence on inclination, in which the migration velocity increased to a maximum and then decreased. Perron et al. [7] further showed that the relationship between terminal velocity and bubble volume varied among four bubble-shape regimes and was especially sensitive to inclination for small bubbles. Behafarid et al. [8] found that the discrepancy between simulated and measured velocities increased with inclination, whereas Liu et al. [9] reported an increase in Taylor-bubble migration velocity as the inclination changed from 0° to 45° in non-Newtonian fluids. More recent visualization experiments have extended these observations to combinations of liquid velocity, viscosity, and inclination [10]. These studies agree that inclination strongly affects bubble migration, but differences in pipe geometry, bubble-to-pipe diameter ratio, bubble shape, and fluid rheology prevent a single inclination–velocity trend from being applied to all systems.

The effects of liquid properties and bubble size have also been examined extensively. Kulkarni and Joshi [11] showed that bubble formation determines the initial bubble size, whereas bubble rise velocity controls the characteristic interphase contact time. For non-Newtonian systems, Wang et al. [12] developed a low-Reynolds-number velocity model for bubbles in yield-stress fluids, and Liu et al. [9] found that increasing liquid viscosity reduced Taylor-bubble migration velocity. Boucher et al. [6] similarly reported that elongated-bubble migration velocity was particularly sensitive to viscosity at small inclination angles. Under deep-water conditions involving hydrate formation, Zhao et al. [13] identified initial bubble size and liquid viscosity as the principal factors controlling migration velocity, whereas liquid density had a comparatively limited effect. Thus, the literature shows broad agreement that increasing viscosity retards bubble migration and that bubble size and deformation influence drag, while the importance of density depends on the specific pressure, temperature, and interfacial conditions.

Existing migration models can be further distinguished by their intended geometries and physical mechanisms. Mitchell and Leonardi [14] developed closure relationships for Taylor bubbles in vertical and inclined annular pipes using the Eötvös, Morton, and Froude numbers. Gao et al. [15] modeled gas migration through undulating sections of horizontal wells by considering density difference, curvature, surface tension, viscosity, and pipe diameter. Lou et al. [16] focused on Taylor bubbles in annular slug flow containing power-law fluids, whereas Ding et al. [17] developed a transient annular-migration model incorporating drag, added-mass, and Basset forces. Zhao et al. [13] additionally considered hydrate phase transition and gas–water mass transfer under deep-water conditions. These models address different bubble forms, fluid rheologies, geometries, and thermodynamic processes and are therefore not directly interchangeable. Their applicability is generally limited to specific flow regimes or operating conditions.

Despite these advances, most existing gas-migration models have been developed from experiments conducted at ambient temperature and pressure and from theoretical correlations derived under corresponding assumptions. In ultra-deep highly deviated and horizontal wells, large variations in pressure and temperature cause substantial changes in the pressure–volume–temperature (PVT) and transport properties of the influx gas. Therefore, gas density, compressibility, and viscosity depend strongly on the local pressure, temperature, and gas composition and should be evaluated using an appropriate equation

of state or thermophysical-property model. Souza-Rêgo et al. [18] investigated the density, compressibility, heat capacities, and other thermodynamic properties of natural-gas mixtures at pressures of 10–60 MPa, while Máximo-Canadas et al. [19] developed a consistent thermophysical-property dataset for methane covering vapor, liquid, and supercritical states. Furthermore, Ranieri et al. [20] experimentally demonstrated a progressive crossover from gas-like to liquid-like molecular diffusion in supercritical methane as pressure and density increased. These findings indicate that the behavior of highly compressed influx gas near the bottomhole may differ substantially from that of gas bubbles under ambient conditions. Nevertheless, the effects of these changing gas properties on migration through ultra-deep highly deviated and horizontal wells have received limited attention.

From an engineering perspective, accurate prediction of gas migration velocity is important for kick detection and well-control operations. Migration velocity determines the location and arrival time of an influx as it moves from the bottomhole toward the riser and surface, thereby affecting the time delay and evolution of pressure, flow-rate, pit-volume, and acoustic responses used for kick identification. Su et al. [21] developed a transient model to predict gas-kick flow behavior by considering wellbore–formation coupling and gas solubility. Yin et al. [22] used multi-source data covering the downhole–riser–surface migration path to establish an early-warning method for gas kicks, while Zhang et al. [23] investigated ultrasonic Doppler monitoring of gas content in deep-water drilling risers. More recently, Wang et al. [24] developed an intelligent kick-detection method combining anomaly detection with parameter-trend analysis. These studies demonstrate the importance of understanding influx propagation for interpreting monitoring signals and determining the available response time. However, existing kick-detection studies have paid comparatively limited attention to the influence of wellbore inclination and highly compressed gas properties on the underlying gas migration velocity. Reliable migration-velocity predictions can therefore provide an important basis for interpreting kick indicators, estimating influx arrival time, and planning subsequent well-control operations.

Because their well sections are extremely long, ultra-deep, highly deviated horizontal wells exhibit large variations in wellbore temperature and pressure, causing pronounced changes in the properties of the influx gas. Near the bottomhole, the methane-rich influx gas may enter a dense, highly compressed state and, under appropriate pressure–temperature conditions, exhibit liquid-like molecular and transport behavior [25,26]. Near the wellhead, the lower temperature and pressure allow it to return to a conventional gaseous state. To represent these changing properties, an adjustable-inclination horizontal-to-vertical multiphase-flow apparatus and corresponding test conditions were designed according to geometric and dynamic similitude, with the Archimedes number (Ar) used as the similarity criterion. The Ar was selected as the primary dynamic-similarity parameter because the migration of bubbles and droplets through a stagnant liquid is driven mainly by the density-difference-induced buoyancy and opposed by viscous resistance. Ar characterizes the relative importance of buoyancy and viscous effects. Unlike the Reynolds number, Ar does not contain the unknown migration velocity and can therefore be specified before the experiment, making it suitable for field-to-laboratory similarity assessment [27,28]. Bubble morphology and migration velocity were investigated at different CMC-adjusted liquid-phase viscosities and wellbore inclinations to characterize gas migration near the wellhead. Oil-droplet morphology and migration velocity were investigated under different HCOOK-solution conditions and wellbore inclinations to characterize gas migration near the bottomhole. Because the addition of HCOOK simultaneously increased the liquid-phase density and viscosity, the oil-droplet experiments represent their coupled effects rather than the isolated effect of density. Parameters for the bubble and oil-droplet migration

velocity models were fitted using more than one hundred experimental datasets, yielding a gas-migration model applicable to ultra-deep highly deviated horizontal wells.

2. Experimental Apparatus and Methods

2.1. Experimental Apparatus

The experimental apparatus was designed to approximate the annular cross-sectional geometry of a representative ultra-deep well. The representative field casing had an outer diameter of 333.4 mm and an inner diameter of 313.6 mm, while the field drill pipe had an outer diameter of 168.3 mm. A nominal diameter-scale ratio of approximately 1:4 was adopted. Accordingly, the experimental wellbore had an inner diameter of 80 mm, and the internal steel pipe representing the drill pipe had an outer diameter of 45 mm. The nominal and actual geometric-scaling ratios are expressed as:

$$\lambda_L \approx 4.0, \quad \lambda_{ci} = \frac{D_{ci,f}}{D_{w,e}} = \frac{313.6}{80} = 3.92, \quad \lambda_{dp} = \frac{D_{dp,f}}{D_{sp,e}} = \frac{168.3}{45} = 3.74 \tag{1}$$

where λ_L is the nominal diameter-scale ratio; λ_{ci} and λ_{dp} are the actual scale ratios based on the casing/wellbore diameter and drill-pipe diameter, respectively; $D_{ci,f}$ is the inner diameter of the field casing; $D_{w,e}$ is the inner diameter of the experimental wellbore; $D_{dp,f}$ is the outer diameter of the field drill pipe; and $D_{sp,e}$ is the outer diameter of the internal steel pipe in the experimental apparatus.

The drill-pipe-to-wellbore diameter ratios were 0.537 for the representative field annulus and 0.563 for the experimental apparatus, corresponding to a relative difference of approximately 4.8%. The annular hydraulic diameters were 145.3 and 35 mm, respectively, giving a hydraulic-diameter scale ratio of 4.15. These values indicate that the apparatus reasonably approximated the cross-sectional geometry of the representative field annulus.

The experimental wellbore was 4 m long, which provided sufficient distance for observing bubble and oil-droplet migration rather than representing a geometrically scaled full well length. Three injection ports, each with an internal diameter of 2 mm, were arranged along the side of the wellbore, and a graduated scale was attached to the outer wall. The wellbore inclination could be adjusted from 0° to 90°, allowing the apparatus to simulate dispersed-phase migration through vertical, highly deviated, and horizontal well sections. The field and experimental geometric parameters are summarized in Table 1.

Table 1. Comparison of representative field and experimental annular geometries.

Parameter	Field Geometry	Experimental Geometry	Scale Ratio
Casing outer diameter	333.4 mm	—	—
Casing/wellbore inner diameter	313.6 mm	80 mm	3.92
Drill-pipe/steel-pipe outer diameter	168.3 mm	45 mm	3.74
Drill-pipe-to-wellbore diameter ratio	0.537	0.563	—
Annular hydraulic diameter	145.3 mm	35 mm	4.15

When influx gas is exposed to the high-temperature, high-pressure environment near the bottomhole, it becomes highly compressed, with a relatively high density and liquid-like properties. To justify using oil droplets as analogs of highly compressed bottomhole gas, dynamic similarity was evaluated using the Archimedes number (Ar), defined as follows:

$$Ar = \frac{g d_e^3 \rho_c (\rho_c - \rho_d)}{\mu_c^2} = \frac{g d_e^3 \Delta\rho}{\rho_c \nu_c^2} \tag{2}$$

where g is gravitational acceleration, m/s^2; ρ_c and ρ_d are the densities of the continuous and dispersed phases, respectively, kg/m^3; μ_c is the dynamic viscosity of the continuous phase, Pa·s; ν_c is the kinematic viscosity of the continuous phase, m^2/s; and d_e is the equivalent diameter of the bubble or oil droplet, m.

Physically, Ar combines gravitational acceleration, dispersed-phase size, continuous-phase density, the density difference between the phases, and continuous-phase viscosity. It therefore represents the relative importance of buoyancy arising from the density difference and viscous effects in the continuous phase. Similarity based on Ar consequently reflects the dynamic similarity between the oil-droplet system and the highly compressed downhole-gas system more effectively than comparison of gas density or phase-density difference alone.

Representative parameters illustrate the rationale for selecting Ar. In the laboratory oil-droplet system, the continuous-phase density was 1300 kg/m^3, its viscosity was 15 mPa·s, the oil-droplet density was 800 kg/m^3, and the equivalent droplet diameter was 5 mm, giving Ar = 3540. For representative downhole conditions, a drilling-fluid density of 1400 kg/m^3, drilling-fluid viscosity of 20 mPa·s, and highly compressed gas density of 150 kg/m^3 [29] were used. Equating the Archimedes numbers of the downhole and laboratory systems gives an equivalent downhole gas-bubble diameter of 4.35 mm. Thus, appropriate adjustment of the continuous-phase properties and oil-droplet size allows the laboratory oil-droplet system to reproduce the relative buoyancy and viscous effects of the highly compressed downhole-gas system, providing a basis for dynamic similitude.

The experimental system consisted of an air compressor, gas valve, gas rotameter, hand pump, liquid mass-flow meter, liquid valve, screw pump, storage tank, circulating wellbore, steel pipe, camera, multiple temperature and pressure sensors, and a data-acquisition system. A schematic of the apparatus is shown in Figure 1. The steel pipe formed an annular flow passage. Liquid entered from the bottom of the wellbore, whereas gas could be injected either at the bottom or at different wellbore heights. Because the wellbore inclination was adjustable, the apparatus could simulate gas migration in vertical, deviated, and horizontal sections under different influx locations, influx rates, and operating conditions.

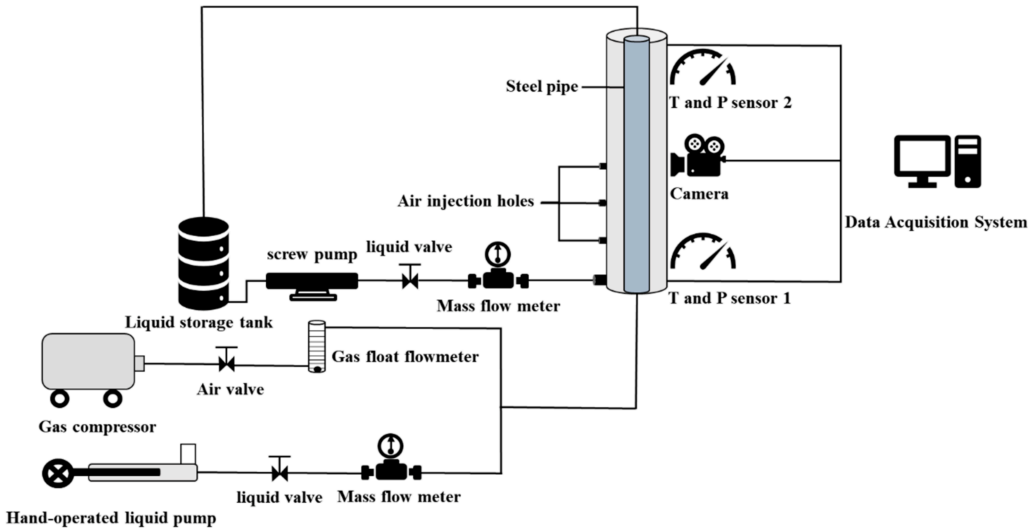


Figure 1. Schematic of the experimental apparatus for ultra-deep highly deviated and horizontal wells.

2.2. Experimental Materials

The experimental materials included purified water; carboxymethyl cellulose (CMC), used primarily to increase liquid viscosity; potassium formate (HCOOK), used to increase

liquid density, with an accompanying increase in viscosity; kerosene; and an oil-soluble dye used to color the kerosene for visualization. The measured physical properties of the experimental fluids are summarized in Table 2.

Table 2. Measured physical properties of the experimental fluids.

Working Fluid	Density/(g·cm^{-3})	Viscosity/(mPa·s)	Supplier
Purified water	1.00	1.0	Laboratory
CMC	1.60	/	Aladdin Reagents (Shanghai) Co., Ltd. (Shanghai, China)
CMC solution 1	1.00	20	/
CMC solution 2	1.00	32	/
CMC solution 3	1.01	56	/
CMC solution 4	1.01	90	/
HCOOK	1.90	/	Aladdin Reagents (Shanghai) Co., Ltd.
HCOOK solution 1	1.1	5	/
HCOOK solution 2	1.2	10	/
HCOOK solution 3	1.3	15	/
HCOOK solution 4	1.4	20	/
Kerosene	0.80	1.2	Aladdin Reagents (Shanghai) Co., Ltd.
Oil-soluble dye	0.85	/	Shanghai McLean Biochemical Technology Co., Ltd. (Shanghai, China)

2.3. Experimental Procedure

(1) Before each test, the storage tank was filled with sufficient purified water, and the liquid pump was started to circulate the water and clean the wellbore;
(2) After cleaning, the storage tank was refilled with a liquid of the required viscosity and density, and the liquid pump was operated until the wellbore liquid became stable;
(3) The wellbore inclination was adjusted to the required test angle using the control panel;
(4) In separate experimental runs, gas bubbles were continuously injected into the wellbore through the injection port using an air compressor, whereas oil droplets were continuously injected using a hand-operated pump;
(5) The bubbles or oil droplets entering the wellbore were recorded with a camera for at least 30 s;
(6) Bubble or oil-droplet injection was stopped, the liquid pump was restarted, and, after the liquid stabilized, steps (3)–(6) were repeated.

2.4. Data Processing

The recorded videos were examined frame by frame to determine the migration time of each bubble or oil droplet. Migration distance was read from the graduated scale, and the velocity of an individual bubble or oil droplet was calculated by dividing distance by time. For each test condition, the velocities of 3–5 bubbles or oil droplets were measured, and their mean was taken as the migration velocity for that condition.

In this study, "migration velocity" is used as the general term for the time-averaged axial velocity of a bubble or oil droplet measured relative to the experimental apparatus. Because the continuous liquid phase was stationary during the migration tests, this velocity was also equal to the dispersed-phase velocity relative to the liquid. "Terminal velocity" refers specifically to the limiting quasi-steady velocity attained by an isolated bubble or droplet when its acceleration becomes negligible, whereas "drift velocity" is retained only when discussing correlations formulated within the drift-flux framework.

3. Experimental Study and Model of Bubble Migration Velocity Under Multiple Influences

After entering the wellbore, gas gradually migrates toward the wellhead and exists in the gaseous phase during this stage. Bubbles were therefore used to investigate migration velocity at liquid-phase viscosities of 1, 20, 32, 56, and 90 mPa·s and wellbore inclinations of 0°, 15°, 30°, 45°, 60°, and 90°. The measured bubble migration velocities are listed in Table 3.

Table 3. Bubble migration velocities at different wellbore inclinations and liquid-phase viscosities.

	0°	15°	30°	45°	60°	90°
1 mPa·s	0.2261	0.2246	0.2200	0.2178	0.1811	0
20 mPa·s	0.1565	0.1322	0.1132	0.0889	0.0697	0
32 mPa·s	0.0475	0.0293	0.0237	0.0158	0.0081	0
56 mPa·s	0.0300	0.0086	0.0063	0.0040	0.0024	0
90 mPa·s	0.0275	0.0053	0.0047	0.0032	0.0015	0

3.1. Effect of Wellbore Inclination on Bubble Migration Velocity

The effect of wellbore inclination on bubble migration velocity was examined at several liquid-phase viscosities. For a representative viscosity of 32 mPa·s, the bubble morphologies at different inclinations are shown in Figure 2. Bubble migration velocities at wellbore inclinations of 0°, 15°, 30°, 45°, and 60° for the different viscosities are shown in Figure 3.

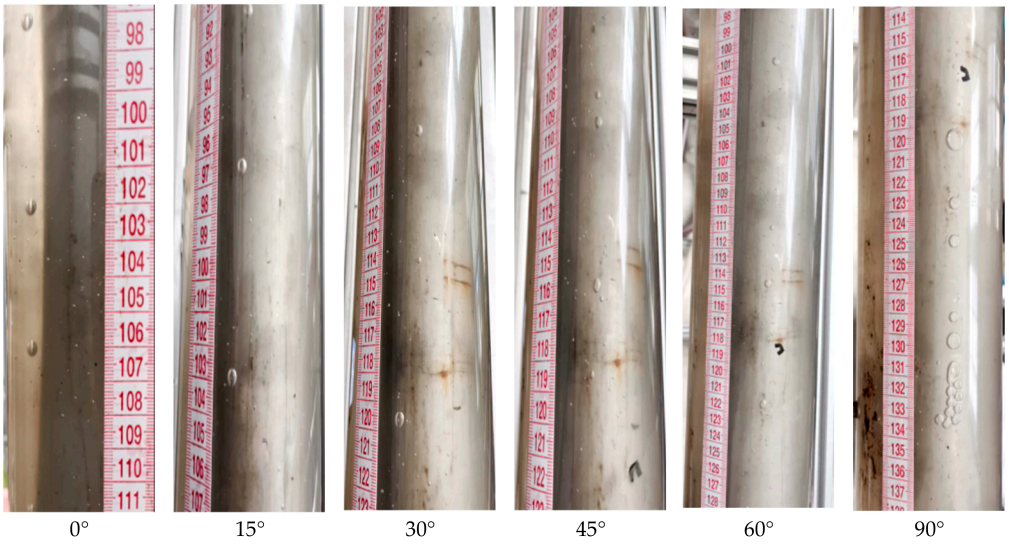


Figure 2. Bubble morphologies at different wellbore inclinations for a liquid-phase viscosity of 32 mPa·s.

As shown in Figure 2, at a wellbore inclination of 0°, buoyancy acts opposite to gravity and is distributed relatively uniformly over the bubble. Because the liquid phase is stagnant, the bubble rises as a relatively regular sphere or near-sphere. As the wellbore changes from vertical to inclined, buoyancy no longer acts along the wellbore axis. The resulting component toward the wall displaces the bubble to one side of the wellbore, and bubble–wall interaction progressively deforms the bubble into an ellipsoidal or irregular shape. In a horizontal wellbore, buoyancy is perpendicular to the axis; bubbles accumulate at the top and form a flattened gas pocket. With no liquid flow, horizontal migration occurs mainly through gas diffusion and interactions among neighboring bubbles, producing a more irregular and dispersed morphology.

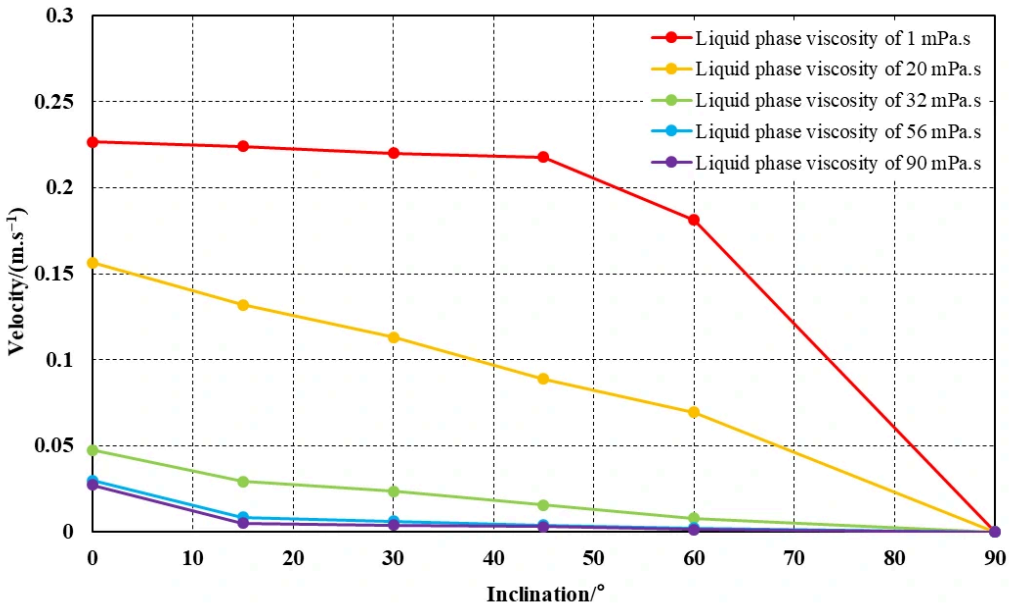


Figure 3. Bubble migration velocity versus wellbore inclination at different liquid-phase viscosities.

As shown in Figure 3, the bubble migration velocity decreased monotonically with increasing wellbore inclination at every liquid-phase viscosity. At 0°, buoyancy acted entirely along the wellbore axis and provided the maximum driving force for upward migration, while the principal resistance was the viscous drag exerted by the continuous liquid phase. As the wellbore inclination increased, the axial component of buoyancy, which is proportional to cosθ, progressively decreased. Meanwhile, the transverse buoyancy component displaced the highly deformable bubbles toward the high side of the wellbore, resulting in asymmetric deformation and stronger wall-confinement and liquid-film effects. Consequently, the axial driving force decreased while the hydrodynamic resistance became more significant, leading to a continuous reduction in bubble migration velocity. In the horizontal wellbore, buoyancy was perpendicular to the wellbore axis, and the principal driving force for axial migration was therefore lost. Any residual axial displacement could arise only from weak diffusion-related redistribution and interactions among neighboring bubbles; no measurable directional migration was observed, and the axial migration velocity was therefore taken as 0 m/s.

3.2. Effect of Liquid-Phase Viscosity on Bubble Migration Velocity

Liquid-phase viscosity was varied by adding CMC to purified water, and its effect on bubble migration velocity was examined at different wellbore inclinations. For a representative inclination of 30°, bubble morphologies at different liquid-phase viscosities are shown in Figure 4. Bubble migration velocities at viscosities of 1, 20, 32, 56, and 90 mPa·s for the different wellbore inclinations are shown in Figure 5.

As shown in Figure 4, increasing the liquid-phase viscosity from 1 to 32 mPa·s progressively increased the viscous resistance and changed the bubble from spherical to ellipsoidal, decreasing its minor-axis dimension and increasing its major-axis dimension. With a further increase in viscosity, the bubble became teardrop-shaped or irregular. At the highest viscosities, some bubbles appeared to be enveloped by a relatively thick liquid layer, forming a shell-like coating. These bubbles could not exchange mass or momentum effectively with the surrounding bubbles or liquid and therefore moved slowly together with the entrained liquid layer.



Figure 4. Bubble morphologies at different liquid-phase viscosities for a wellbore inclination of 30°.

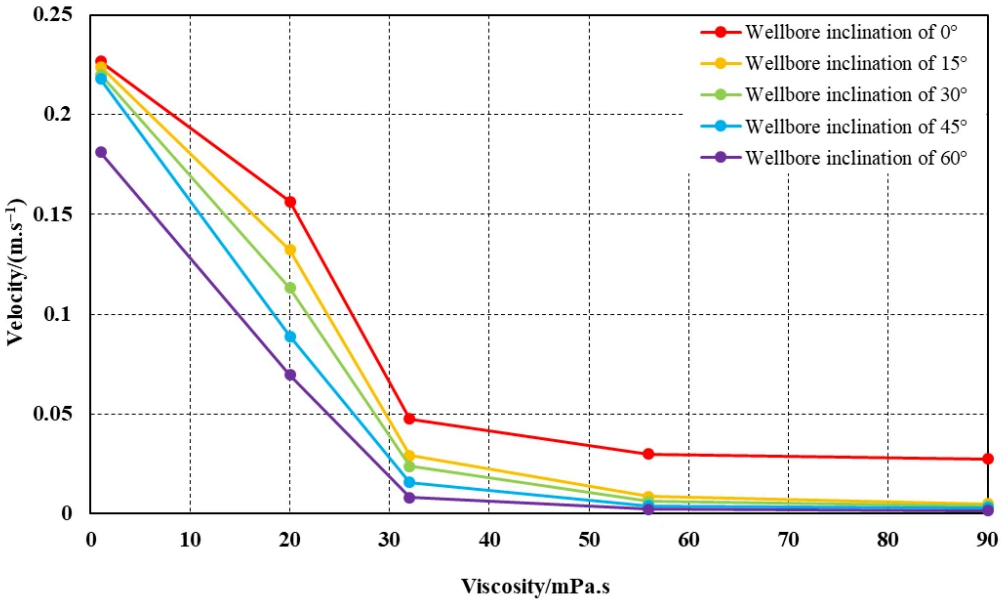


Figure 5. Bubble migration velocity versus liquid-phase viscosity at different wellbore inclinations.

As shown in Figure 5, bubble migration velocity decreased monotonically with increasing liquid-phase viscosity at every wellbore inclination because viscous resistance increased. At low viscosity, bubbles readily collided and coalesced during ascent, forming larger bubbles. As viscosity increased, collision and coalescence became less frequent, resulting in a more uniform bubble-size distribution but a nonuniform spatial distribution. When the inclination was less than 30°, migration velocity decreased rapidly with increasing viscosity; at inclinations greater than 30°, the decrease was more gradual. This behavior is attributed to buoyancy being much greater than resistance below 30°, whereas at larger inclinations the reduced buoyancy component becomes comparable to the resistance and migration slows markedly.

3.3. Bubble Migration Velocity Model Considering Wellbore Inclination, Liquid-Phase Viscosity, and Bubble Size

The experimental results show that bubble migration in a wellbore is governed by several factors, including wellbore inclination, liquid-phase viscosity, and bubble diameter

and shape. The terminal rise velocity is reached when the forces on the bubble are in equilibrium. A bubble-rise-velocity equation can therefore be derived from a force balance. The forces acting on a bubble in a conventional vertical well are illustrated in Figure 6.

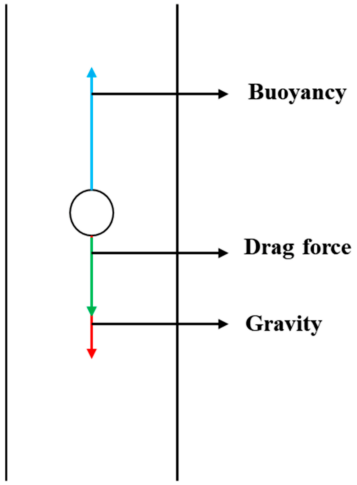


Figure 6. Force balance for bubble migration in a vertical well.

The principal forces acting on a bubble in the liquid phase are gravity, buoyancy, and drag, expressed as follows:

Gravity:

$$G = \frac{1}{6}\pi d_e^3 \rho_g g \tag{3}$$

Buoyancy:

$$F_1 = \frac{1}{6}\pi d_e^3 \rho_l g \tag{4}$$

Drag:

$$F_2 = \frac{1}{8}\pi d_e^2 C_D \rho_l v_g^2 \tag{5}$$

Force equilibrium gives:

$$F_1 = G + F_2 \tag{6}$$

Simplification gives the bubble migration velocity in a vertical well:

$$v_g = \sqrt{\frac{4 g d_e (\rho_l - \rho_g)}{3 \rho_l C_D}} \tag{7}$$

where ρ_g is the gas density, kg/m^3; ρ_l is the liquid-phase density, kg/m^3; C_D is the drag coefficient; and v_g is the bubble migration velocity, m/s.

The same force-balance approach gives the bubble migration velocity in a highly deviated well. The corresponding force diagram is shown in Figure 7.

The acting forces remain gravity, buoyancy, and drag, expressed as follows:

Gravity:

$$G' = \frac{1}{6}\pi d_e^3 \rho_g g \cos\theta \tag{8}$$

Buoyancy:

$$F_1' = \frac{1}{6}\pi d_e^3 \rho_l g \cos\theta \tag{9}$$

Drag:

$$F_2' = \frac{1}{8}\pi d_e^2 C_D' \rho_l v_g^2 \tag{10}$$

Force equilibrium gives:

$$F_1' = G' + F_2' \tag{11}$$

Simplification gives the bubble migration velocity in a highly deviated well:

$$v_g = \sqrt{\frac{4gd_e \cos\theta(\rho_l - \rho_g)}{3\rho_l C_D'}} \tag{12}$$

where C_D is the drag coefficient for a highly deviated well, and θ is the wellbore inclination, °.

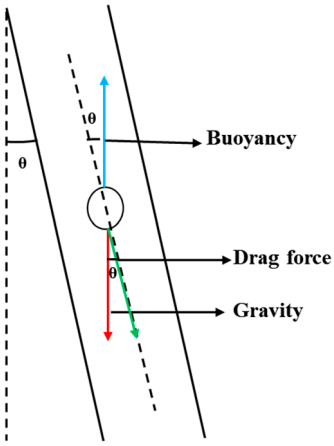


Figure 7. Force balance for bubble migration in a highly deviated well.

Determination of the drag coefficient is central to the bubble migration velocity model. Accounting for surface tension, viscosity, density, bubble diameter, and bubble rise velocity, the drag coefficient for a bubble rising through a liquid can be written in the following functional form:

$$C_D = k\rho_l^a \sigma^b \mu^c d^d v_g^e g^f \tag{13}$$

Dimensional analysis gives:

$$C_D = k\left(\frac{\rho_l d_e v_g}{\mu_l}\right)^e \left(\frac{\rho_l^2 g d_e^3}{\mu_l^2}\right)^{(a+b-e)/2} \left(\frac{\rho_l g d_e^2}{\sigma}\right)^{-b} \tag{14}$$

The dimensionless groups are defined as follows:

$$C_D = B_1 \mathrm{Re}^{B_2} Ar^{B_3} Eo^{B_4} \tag{15}$$

where $\mathrm{Re} = \frac{\rho_l d_e v_g}{\mu_l}$ is the Reynolds number; $Eo = \frac{\rho_l g d_e^2}{\sigma}$ is the Eötvös number; σ is the gas–liquid interfacial tension, N/m; and μ_l is the liquid-phase viscosity, Pa·s.

Fitting 155 experimental datasets gives the following expression for the drag coefficient C_D:

$$C_D = 59.7\mathrm{Re}^{-1.58} Ar^{0.323} Eo^{0.262} \tag{16}$$

Comparison of values calculated with the fitted C_D correlation against the experimental measurements shows deviations of approximately 20%. The comparison is presented in Figure 8, and the fitted correlation has $R^2 = 0.924$.

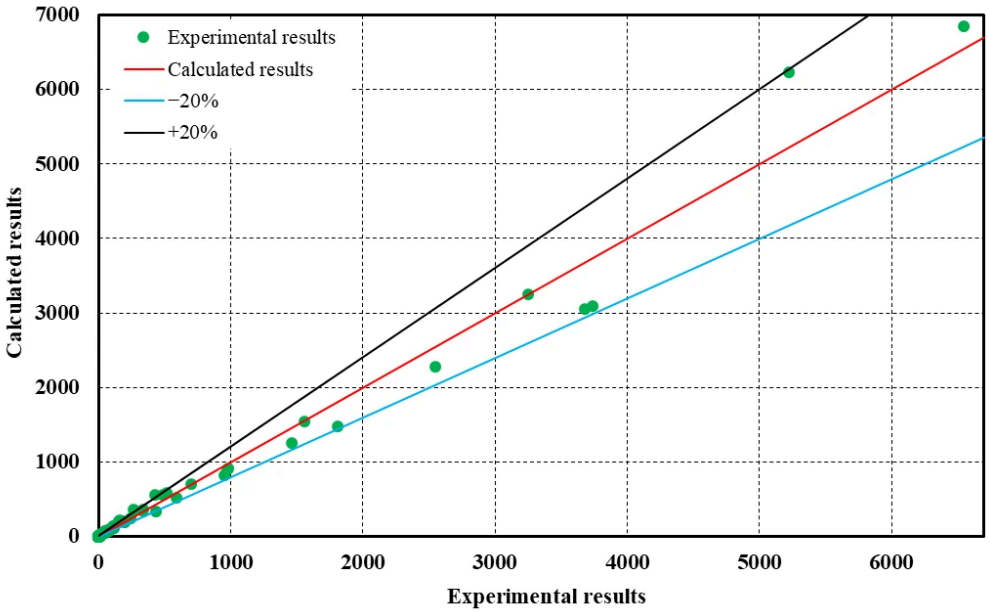


Figure 8. Comparison of calculated and measured C_D.

The resulting bubble migration velocity model, incorporating wellbore inclination, liquid-phase viscosity, and bubble size, is:

$$\begin{cases} v_g = \sqrt{\frac{4gd_e \cos\theta(\rho_l - \rho_g)}{3\rho_l C_D}} \\ C_D = 59.7\mathrm{Re}^{-1.58} Ar^{0.323} Eo^{0.262} \end{cases} \quad (17)$$

4. Experimental Study and Model of Oil-Droplet Migration Velocity Under Multiple Influences

Oil droplets were therefore used to investigate migration velocity under five paired liquid-phase density–viscosity conditions: 1.00 g·cm^{-3} and 1 mPa·s, 1.10 g·cm^{-3} and 5 mPa·s, 1.20 g·cm^{-3} and 10 mPa·s, 1.30 g·cm^{-3} and 15 mPa·s, and 1.40 g·cm^{-3} and 20 mPa·s. The investigated wellbore inclinations were 0°, 15°, 30°, 45°, 60°, and 90°. The measured velocities are listed in Table 4.

Table 4. Oil-droplet migration velocities at different wellbore inclinations and paired liquid-phase density–viscosity conditions.

Density	Viscosity	0°	15°	30°	45°	60°	90°
1 g/cm^3	1 mPa·s	0.1178	0.1201	0.1321	0.1023	0.0786	0
1.1 g/cm^3	5 mPa·s	0.1310	0.1393	0.1449	0.1269	0.1091	0
1.2 g/cm^3	10 mPa·s	0.1420	0.1432	0.1526	0.1316	0.1093	0
1.3 g/cm^3	15 mPa·s	0.1300	0.1385	0.1299	0.1156	0.0924	0
1.4 g/cm^3	20 mPa·s	0.1345	0.1456	0.1358	0.1265	0.1044	0

4.1. Effect of Wellbore Inclination on Oil-Droplet Migration Velocity

The effect of wellbore inclination on oil-droplet migration velocity was examined separately under five paired liquid-phase density–viscosity conditions. Because the liquid properties remained fixed within each inclination series, the inclination effect could be evaluated for each test fluid. For the representative condition of density of 1.3 g·cm^{-3} and viscosity of 15 mPa·s, the oil-droplet morphologies at different inclinations are shown in Figure 9. The migration velocities measured at different inclinations under all five liquid conditions are shown in Figure 10.

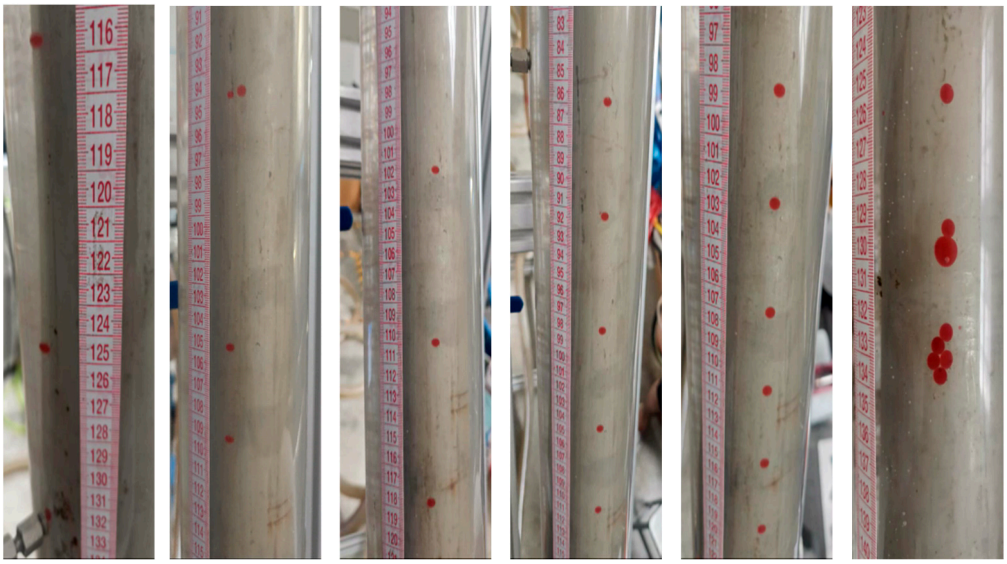


Figure 9. Oil-droplet morphologies at different wellbore inclinations for a liquid-phase density of 1.30 g·cm^{-3} and viscosity of 15 mPa·s.

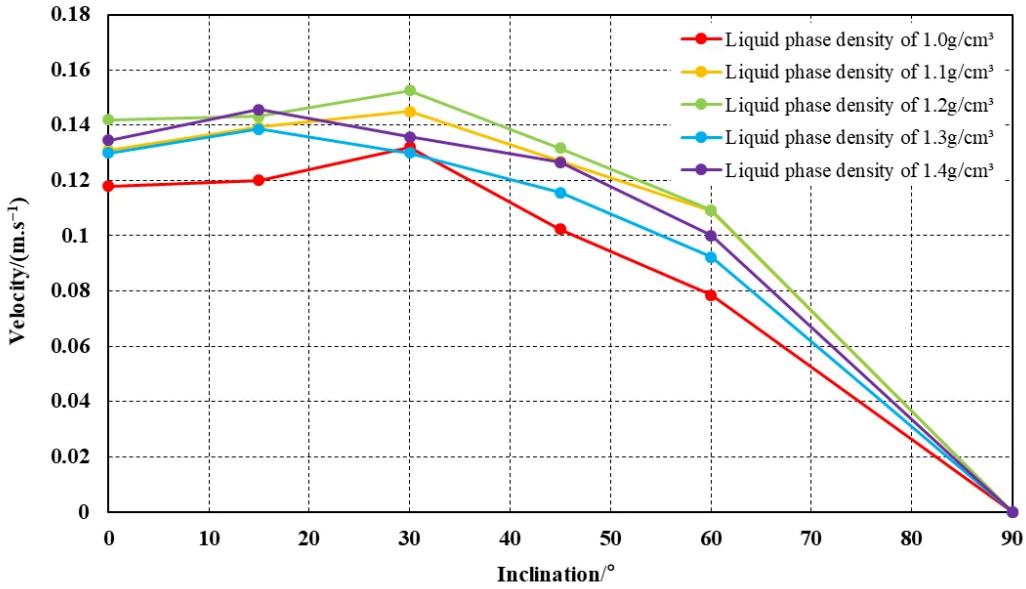


Figure 10. Oil-droplet migration velocity versus wellbore inclination under different paired liquid-phase density–viscosity conditions.

As shown in Figure 9, at a wellbore inclination of 0°, oil droplets migrated vertically upward under buoyancy. The liquid resistance was relatively uniform in all directions, and the droplets remained nearly spherical. As inclination increased, the migration path along the wellbore lengthened, the droplets shifted toward the lower side of the wellbore, and their shape became ellipsoidal. Near the horizontal orientation, the angle between buoyancy and the wellbore axis increased. The droplets migrated horizontally along the upper crest (high side) of the wellbore, exhibiting severe flattening into disk-like or ribbon-like morphologies.

As shown in Figure 10, the oil-droplet migration velocity first increased and then decreased with increasing wellbore inclination under every paired density–viscosity condition. Under the conditions of 1.00–1.20 g·cm^{-3} and 1–10 mPa·s, the maximum velocity occurred at 30°, whereas under the conditions of 1.30–1.40 g·cm^{-3} and 15–20 mPa·s, the maximum shifted to 15°. This shift should be interpreted as the response to the coupled

changes in liquid density and viscosity rather than to density alone. From 0° to the critical inclination, the normal buoyancy component drives droplets toward the high side of the conduit, establishing an eccentric drainage corridor for the continuous liquid phase. The resulting reduction in frontal hydraulic drag exceeds the attenuation of axial buoyancy, accelerating droplet ascent. With a further increase in inclination, the angle between the resultant buoyancy–gravity force and the wellbore axis increases, decreasing the axial driving component. At the same time, the nearly horizontal motion encounters greater liquid resistance. At 90°, buoyancy is almost perpendicular to the wellbore axis, the axial driving component approaches zero, and the larger liquid contact area requires more liquid to be displaced; the migration velocity therefore approaches zero.

4.2. Effect of HCOOK Concentration on Oil-Droplet Morphology and Migration Velocity

The properties of the continuous liquid phase were varied by adding different concentrations of HCOOK to purified water. Increasing the HCOOK concentration simultaneously increased both the density and viscosity of the solution. Therefore, HCOOK concentration is used as the independent variable in Figures 11 and 12, while the resulting changes in oil-droplet behavior are interpreted as the coupled response to the simultaneous variations in liquid density and viscosity.

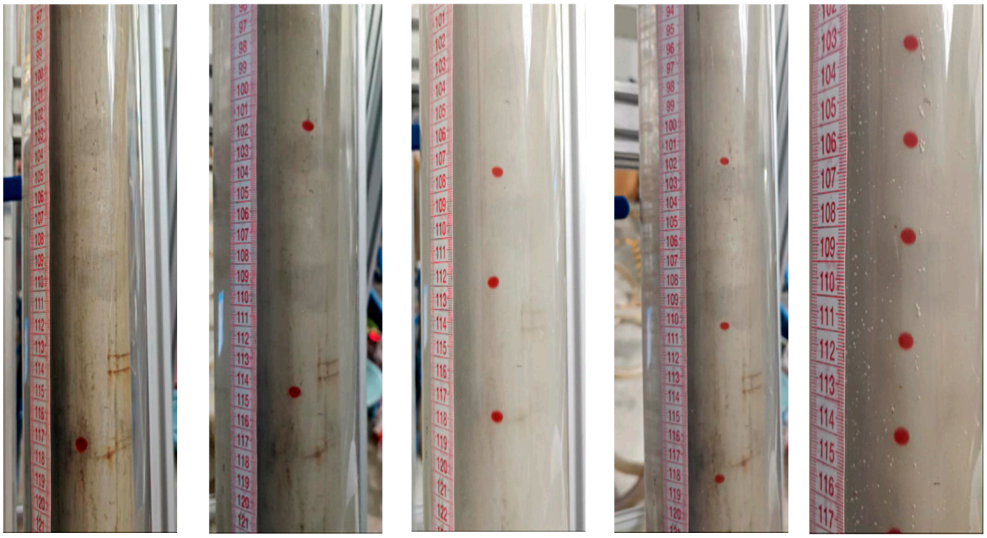


Figure 11. Oil-droplet morphologies at different HCOOK concentrations at a wellbore inclination of 30°.

As shown in Figure 11, the simultaneous increases in liquid-phase density and viscosity produced no appreciable overall change in oil-droplet morphology. Increasing density enlarged the phase-density difference and enhanced buoyancy, whereas the accompanying increase in viscosity strengthened the viscous resistance. The competition between these effects allowed a new force balance to develop, and the droplet morphology consequently remained relatively stable over the investigated HCOOK-solution conditions.

As shown in Figure 12, the oil-droplet migration velocity varied non-monotonically with increasing HCOOK concentration at every wellbore inclination. Increasing the HCOOK concentration simultaneously increased the continuous-phase density and viscosity. The increase in density enlarged the phase-density difference and enhanced the buoyancy force, whereas the accompanying increase in viscosity increased the hydrodynamic drag. The observed velocity trend therefore reflects the competition between buoyancy enhancement and viscous retardation and cannot be attributed to either density

or viscosity alone. Similarly, the shift in the inclination corresponding to the maximum velocity reflects the coupled influence of these two properties.

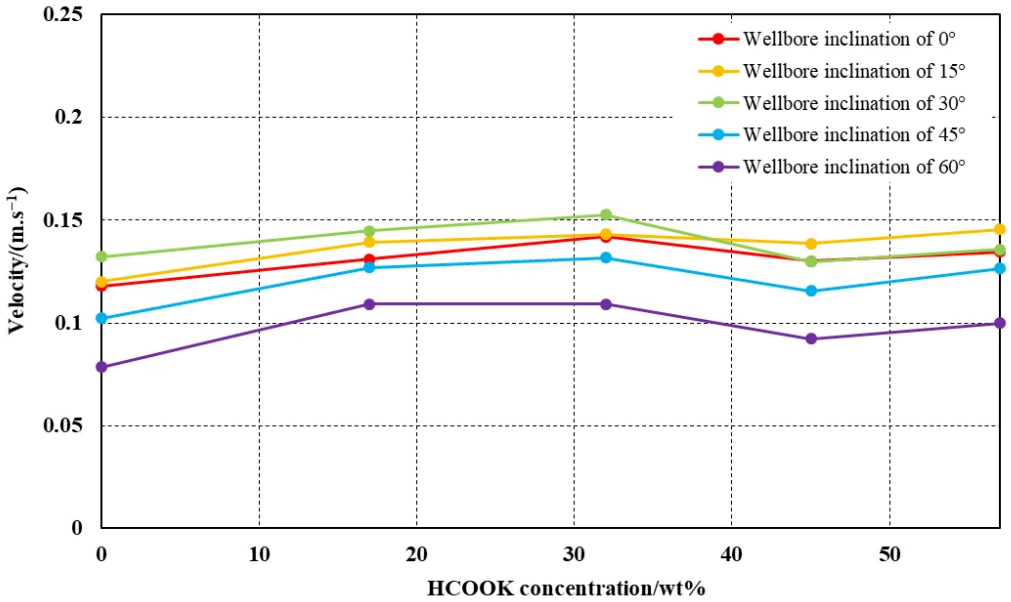


Figure 12. Oil-droplet migration velocity versus HCOOK concentration at different wellbore inclinations.

4.3. Oil-Droplet Migration Velocity Model Considering Wellbore Inclination, Liquid-Phase Density and Viscosity, and Oil-Droplet Size

As in the small-bubble model, an oil-droplet rise-velocity equation was derived from a force balance:

$$v_o = \sqrt{\frac{4gd_e \cos\theta(\rho_l - \rho_o)}{3\rho_l C_D'}} \tag{18}$$

where C_D' is the drag coefficient for oil-droplet migration, and ρ_o is the oil-droplet density, kg/m^3.

Similar to the case of gas, we use dimensionless parameters such as Re, Ar, and Eo to obtain the form of the drag coefficient for oil droplets:

$$C_D' = \begin{cases} 41.8947 Re^{-1.30133} Ar^{0.121329} Eo^{0.471497}, & \text{Re} \le 62 \\ 1.30516 Re^{-0.672521} Ar^{0.343218} Eo^{-0.221216}, & \text{Re} > 62 \end{cases} \tag{19}$$

Comparison of values calculated with the fitted C_D' correlation against the experimental measurements shows deviations of approximately 20%. The comparison is presented in Figure 13, and the fitted correlation has $R^2 = 0.966$.

The resulting oil-droplet migration velocity model, incorporating wellbore inclination, density, viscosity, and oil-droplet size, is:

$$\begin{cases} v_o = \sqrt{\frac{4gd_e \cos\theta(\rho_l - \rho_o)}{3\rho_l C_D}} \\ C_D' \begin{cases} 41.8947 Re^{-1.30133} Ar^{0.121329} Eo^{0.471497}, & \text{Re} \le 62 \\ 1.30516 Re^{-0.672521} Ar^{0.343218} Eo^{-0.221216}, & \text{Re} > 62 \end{cases} \end{cases} \tag{20}$$

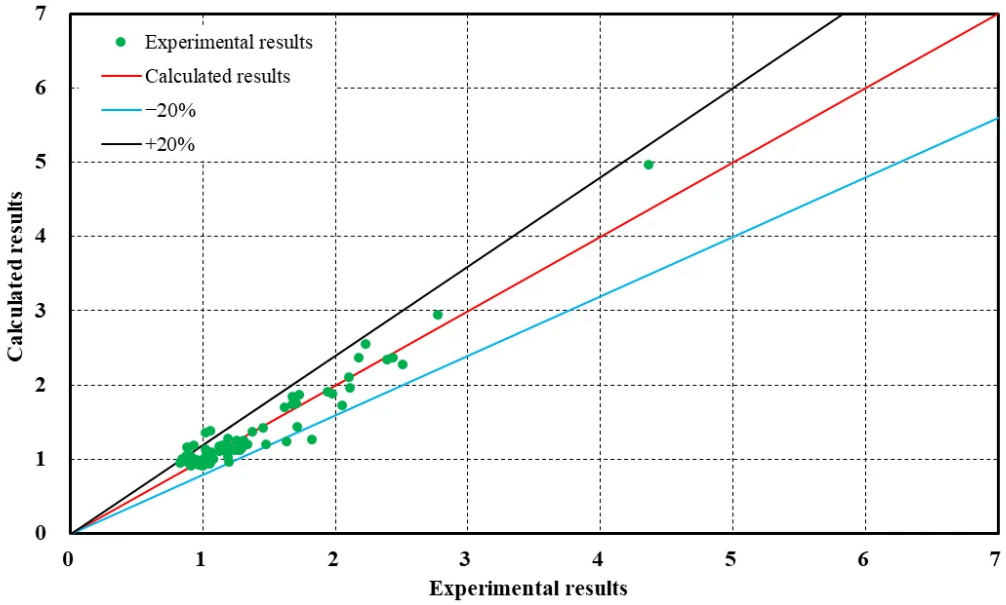


Figure 13. Comparison of calculated and measured C_D'.

5. Model Validation

The migration velocity model developed in this study was validated against several field cases. The basic parameters of the three field example wells are summarized in Table 5. The calculated results agreed well with the field data, with absolute relative errors below 15%, indicating practical engineering value. For application, the wellbore temperature and pressure distributions are first calculated, and gas density is then obtained from an equation of state. The gas in a wellbore section is classified as highly compressed when its density exceeds the critical density; the oil-droplet model is used for such a section, whereas the bubble model is used otherwise. The critical density refers to the thermodynamic critical density of the influx gas. For methane, for example, the critical density is 162.66 kg/m^3. The wellbore is divided into equal-length sections; the appropriate model is used to calculate the migration velocity and travel time in each section, and the section travel times are summed. The total measured depth divided by the total travel time gives the average gas migration velocity.

The calculated results were compared with both field data and classical baseline correlations, as shown in Table 6. The three classical correlations were included as historical baselines rather than as fully equivalent models for inclined annular wellbores. The Hu–Kintner [30] and Ishii–Zuber [31] correlations do not explicitly include wellbore inclination, whereas the Masliyah–Jauhari–Gray [32] correlation accounts for inclination but was developed for bubbles moving along an inclined flat surface. Accordingly, their predictions for Example Well 3 are presented only to indicate the differences between conventional drag-based correlations and the present inclination-dependent annular-wellbore model.

Table 5. Basic parameters of the field wells used for model validation.

Parameter	Example Well 1	Example Well 2	Example Well 3
Measured depth/m	6569.00	5941.95	8697.00
True vertical depth/m	6018.23	5656.32	8505.00
Maximum inclination/°	62.50	70.50	84.99
Hole diameter/mm	168.30	171.50	168.30
Downhole pressure/MPa	113.35	66.59	116.81
Downhole temperature/°C	202.50	217.30	280.15

Table 6. Comparison of model-calculated average gas migration velocities with field measurements and model predictions.

Case/Model	Migration Distance/m	Migration Time/s	Measured or Other-Model Velocity/(m·s^{-1})	Present-Model Velocity/(m·s^{-1})	Relative Error/%
Example Well 1	1081	10620	0.1018	0.1132	11.20
Example Well 2	1620.63	6360	0.2548	0.2325	8.75
Example Well 3	698.37	4860	0.1437	0.1585	10.30
Hu–Kintner [30]	698.37	4860	0.1897	0.1585	32.01
Ishii–Zuber [31]	698.37	4860	0.1780	0.1585	23.87
Masliyah–Jauhari–Gray [32]	698.37	4860	0.1688	0.1585	17.47
Liu [33]	698.37	4860	0.1698	0.1585	18.16

6. Conclusions

This study addresses the occurrence of influx gas in conventional gaseous and highly compressed states as wellbore temperature and pressure change along ultra-deep, highly deviated, and horizontal wells. Bubbles and oil droplets were used as physical analogs of the two states, respectively. Adjustable-inclination annular experiments were conducted to investigate the effects of liquid properties and wellbore inclination on migration behavior. Corresponding migration velocity models were developed from force balances and dimensionless analysis and were further validated against field cases. The main conclusions are as follows:

(1) As the wellbore changed from vertical to horizontal, bubbles evolved from nearly spherical to ellipsoidal and irregular flattened shapes. At the same time, the effective buoyancy component along the wellbore axis decreased, whereas wall effects and viscous resistance became relatively more important; consequently, bubble migration velocity decreased monotonically with increasing inclination. Increasing liquid-phase viscosity further increased viscous resistance and suppressed bubble collision, coalescence, and interfacial renewal, so migration velocity decreased with viscosity at every inclination.

(2) With increasing wellbore inclination, the oil droplets evolved from nearly spherical to ellipsoidal and flattened shapes, while their migration velocity first increased and then decreased. Under the paired conditions of 1.00–1.20 g·cm^{-3} and 1–10 mPa·s, the maximum measured velocity occurred near 30°; under the paired conditions of 1.30–1.40 g·cm^{-3} and 15–20 mPa·s, the maximum shifted to approximately 15°. This behavior differed from the monotonic decrease observed for gas bubbles because the two dispersed phases exhibited different deformation and wall-interaction characteristics. For the oil droplets, a moderate inclination promoted eccentric migration and the formation of a preferential drainage corridor, reducing the migration resistance sufficiently to offset the decrease in the axial buoyancy component. At larger inclinations, the continued reduction in axial buoyancy and the increasing wall-related resistance became dominant, causing the oil-droplet velocity to decrease.

(3) Increasing the HCOOK concentration simultaneously increased the liquid-phase density and viscosity. Although the oil-droplet morphology changed little overall, the migration velocity varied non-monotonically because increasing density enhanced buoyancy while increasing viscosity strengthened hydrodynamic drag. The observed velocity variation and the shift in the critical inclination therefore reflect the coupled effects of density and viscosity rather than an isolated density effect.

(4) The bubble and oil-droplet migration models were developed separately from force balances and dimensionless analysis. Their drag-coefficient correlations incorporate

Re, Ar, and Eo to represent the coupled effects of viscous resistance, buoyancy, density difference, dispersed-phase size, and interfacial forces. Within the investigated experimental ranges, the deviations between the calculated and measured migration velocities were approximately 20%. The two separate correlations therefore constitute a combined modeling framework in which the appropriate model is selected for each wellbore section according to the gas-state switching criterion described in Section 5.

(5) For field application, the local gas state is determined from the wellbore pressure and temperature distributions and from the corresponding gas properties calculated using an appropriate equation of state. The oil-droplet model is applied when the calculated gas density exceeds the composition-specific critical density, whereas the bubble model is applied otherwise. The migration times calculated for individual wellbore sections are accumulated to determine the average migration velocity over the entire well. For the three field cases examined, the relative errors between the predicted and measured migration velocities ranged from 8.75% to 11.20%, supporting the applicability of the proposed model under the investigated conditions. The proposed model can provide useful guidance for estimating gas migration velocity and migration time in field well-control calculations.

Author Contributions: Conceptualization, X.Z.; Methodology, X.Z., Y.L. and H.Q.; Software, H.Y.; Formal analysis, H.Q.; Investigation, Y.L.; Data curation, H.Y.; Writing—original draft, X.Z. and H.Q.; Writing—review and editing, Y.L. and H.Y.; Visualization, H.Y.; Supervision, Y.L. All authors have read and agreed to the published version of the manuscript.

Funding: The authors greatly acknowledge the financial support from the National Natural Science Foundation of China Centre for Basic Science Project (Grant NOs. 52288101).

Data Availability Statement: The data presented in this study are available on request from the corresponding author.

Conflicts of Interest: Authors Xuliang Zhang and Hao Qin were employed by the PetroChina Tarim Oilfield Company. The remaining authors declare that the research was conducted in the absence of any commercial or financial relationships that could be construed as a potential conflict of interest. The PetroChina Tarim Oilfield Company had no role in the design of the study; in the collection, analyses, or interpretation of data; in the writing of the manuscript; or in the decision to publish the results.

References

1. Wang, H.; Huang, H.; Bi, W.; Ji, G.; Zhou, B.; Zhuo, L. Deep and ultra-deep oil and gas well drilling technologies: Progress and prospect. *Nat. Gas. Ind. B* **2022**, *9*, 141–157. [CrossRef]
2. Wang, H.; Huang, H.; Ji, G.; Chen, C.; Lv, Z.; Chen, W.; Bi, W.; Liu, L. Progress and challenges of drilling and completion technologies for deep, ultra-deep and horizontal wells of CNPC. *China Pet. Explor.* **2023**, *28*, 1.
3. Zhang, Y.; Li, M.; Zhao, Q.; Song, X.; Zhang, R.; Yang, L. Wellbore pressure model for drilling fluid in ultra-deep rock salt formations at high temperatures and pressures. *Phys. Fluids* **2024**, *36*, 023341. [CrossRef]
4. Shosho, C.E.; Ryan, M.E. An experimental study of the motion of long bubbles in inclined tubes. *Chem. Eng. Sci.* **2001**, *56*, 2191–2204. [CrossRef]
5. Massoud, E.; Xiao, Q.; El-Gamal, H. Numerical study of an individual Taylor bubble drifting through stagnant liquid in an inclined pipe. *Ocean Eng.* **2020**, *195*, 106648. [CrossRef]
6. Boucher, A.; Karp, J.; Belt, R.; Liné, A. Dynamics of elongated bubbles in slightly inclined pipes with viscous fluids. *J. Fluid Mech.* **2023**, *977*, A40. [CrossRef]
7. Perron, A.; Kiss, L.; Poncsak, S. An experimental investigation of the motion of single bubbles under a slightly inclined surface. *Int. J. Multiph. Flow* **2006**, *32*, 606–622. [CrossRef]
8. Behafarid, F.; Jansen, K.; Podowski, M. A study on large bubble motion and liquid film in vertical pipes and inclined narrow channels. *Int. J. Multiph. Flow* **2015**, *75*, 288–299. [CrossRef]

9. Liu, Y.; Upchurch, E.R.; Ozbayoglu, E.M. Experimental study of single Taylor bubble rising in stagnant and downward flowing non-Newtonian fluids in inclined pipes. *Energies* **2021**, *14*, 578. [CrossRef]
10. Yin, B.; Ding, T.; Ren, M.; Wang, Z.; Sun, B.; Wang, L. Development and application of a visual observation device for measuring bubble migration characteristics. *Exp. Technol. Manag.* **2024**, *41*, 180–185.
11. Kulkarni, A.A.; Joshi, J.B. Bubble formation and bubble rise velocity in gas–liquid systems: A review. *Ind. Eng. Chem. Res.* **2005**, *44*, 5873–5931. [CrossRef]
12. Wang, Z.; Lou, W.; Sun, B.; Pan, S.; Zhao, X.; Liu, H. A model for predicting bubble velocity in yield-stress fluid at low Reynolds number. *Chem. Eng. Sci.* **2019**, *201*, 325–338. [CrossRef]
13. Zhao, X.; Yin, F.; Yao, H.; Qi, Y.; Cao, X. A new model of bubble migration velocity in deep-water wellbore considering hydrate phase transition. *J. Mar. Sci. Eng.* **2023**, *11*, 2206. [CrossRef]
14. Mitchell, T.; Leonardi, C. Development of closure relations for the motion of Taylor bubbles in vertical and inclined annular pipes using high-fidelity numerical modeling. *Phys. Fluids* **2020**, *32*, 063306. [CrossRef]
15. Gao, Y.; Sun, X.; Zhao, T.; Wang, Z.; Zhao, X.; Sun, B. Study on the migration of gas kicks in undulating sections of horizontal wells. *Int. J. Heat Mass Transf.* **2018**, *127*, 1161–1167. [CrossRef]
16. Lou, W.; Wang, Z.; Guo, B.; Pan, S.; Liu, Y.; Sun, B. Numerical analysis of velocity field and energy transformation, and prediction model for Taylor bubbles in annular slug flow of static power-law fluid. *Chem. Eng. Sci.* **2022**, *250*, 117396. [CrossRef]
17. Ding, L.; Zhu, H.; Chen, W.; Liu, Y.; Zhang, Q. Study on transient migration characteristics of leaking bubble in gas well annulus. *China Saf. Sci. J.* **2023**, *33*, 89.
18. Souza-Rêgo, J.J.F.; Borges, I.; Alves, L.; Pereira, L.O.V.; Ramos, R.; Nichele, J. Thermodynamic properties of natural gas mixture in the pre-salt layer: A molecular dynamics approach. *Chem. Eng. Sci.* **2025**, *312*, 121505. [CrossRef]
19. Máximo-Canadas, M.; Souza, R.C.; Duarte, J.C.; Nichele, J.; Alves, L.; Pereira, L.O.V.; Franco, L.G.; Borges, I., Jr. Consistent set of thermophysical properties of methane curated with machine learning. *Phys. Rev. E* **2025**, *112*, 045427. [CrossRef] [PubMed]
20. Ranieri, U.; Formisano, F.; Gorelli, F.A.; Santoro, M.; Koza, M.M.; De Francesco, A.; Bove, L.E. Crossover from gas-like to liquid-like molecular diffusion in a simple supercritical fluid. *Nat. Commun.* **2024**, *15*, 4142. [CrossRef] [PubMed]
21. Su, Y.; Ma, H.; Xia, L.; Peng, C.; Guo, J.; Shen, X.; Fu, J.; Tang, Y. Prediction and analysis of flow behavior during gas kicks considering wellbore–formation coupling and gas solubility. *Front. Earth Sci.* **2025**, *13*, 1558305. [CrossRef]
22. Yin, Q.; Zhu, Q.; Song, Z.; Guo, Y.; Yang, J.; Xu, Z.; Chen, K.; Sun, L.; Tyagi, M. Deep learning based early warning methodology for gas kick of deepwater drilling using pilot-scale rig data. *Process Saf. Environ. Prot.* **2025**, *196*, 106844. [CrossRef]
23. Zhang, Z.; Yin, X.; Sun, C.; Zhang, H.; Wei, Z.; Ma, G.; Li, W.; Li, X.; Yuan, X. Gas kick monitoring in deep-water drilling risers based on ultrasonic Doppler spectroscopy. *Ocean Eng.* **2025**, *321*, 120457. [CrossRef]
24. Wang, B.; Yang, H.; Li, J.; Liu, G.; Zhang, G.; Zhan, J.; Long, Z. An intelligent kick detection method integrating anomaly detection with parameter trends. *Process Saf. Environ. Prot.* **2026**, *211*, 108790. [CrossRef]
25. Smith, D.; Hakeem, M.A.; Parisiades, P.; Maynard-Casely, H.E.; Foster, D.; Eden, D.; Bull, D.J.; Marshall, A.R.L.; Adawi, A.M.; Howie, R.; et al. Crossover between liquidlike and gaslike behavior in CH_4 at 400 K. *Phys. Rev. E* **2017**, *96*, 052113. [CrossRef] [PubMed]
26. Ranieri, U.; Klotz, S.; Gaal, R.; Koza, M.M.; Bove, L.E. Diffusion in dense supercritical methane from quasi-elastic neutron scattering measurements. *Nat. Commun.* **2021**, *12*, 1958. [CrossRef] [PubMed]
27. Quan, S. Co-current flow effects on a rising Taylor bubble. *Int. J. Multiph. Flow* **2011**, *37*, 888–897. [CrossRef]
28. Tripathi, M.K.; Sahu, K.C.; Govindarajan, R. Dynamics of an initially spherical bubble rising in quiescent liquid. *Nat. Commun.* **2015**, *6*, 6268. [CrossRef] [PubMed]
29. Cristancho, D.E.; Mantilla, I.D.; Ejaz, S.; Hall, K.R.; Atilhan, M.; Iglesia-Silva, G.A. Accurate PρT data for methane from (300 to 450) K up to 180 MPa. *J. Chem. Eng. Data* **2010**, *55*, 826–829. [CrossRef]
30. Hu, S.; Kintner, R.C. The fall of single liquid drops through water. *AIChE J.* **1955**, *1*, 42–48. [CrossRef]
31. Ishii, M.; Zuber, N. Drag coefficient and relative velocity in bubbly, droplet or particulate flows. *AIChE J.* **1979**, *25*, 843–855. [CrossRef]
32. Masliyah, J.; Jauhari, R.; Gray, M. Drag coefficients for air bubbles rising along an inclined surface. *Chem. Eng. Sci.* **1994**, *49*, 1905–1911. [CrossRef]
33. Liu, Y.; Upchurch, E.R.; Ozbayoglu, E.M. Experimental and theoretical studies on Taylor bubbles rising in stagnant non-Newtonian fluids in inclined non-concentric annuli. *Int. J. Multiph. Flow* **2022**, *147*, 103912. [CrossRef]

Disclaimer/Publisher's Note: The statements, opinions and data contained in all publications are solely those of the individual author(s) and contributor(s) and not of MDPI and/or the editor(s). MDPI and/or the editor(s) disclaim responsibility for any injury to people or property resulting from any ideas, methods, instructions or products referred to in the content.